Lasing in subwavelength semiconductor nanopatches

2011 Semicond. Sci. Technol. 26 014013

(http://iopscience.iop.org/0268-1242/26/1/014013)

Semicond. Sci. Technol. **26** (2011) 014013 (8pp) doi:10.1088/0268-1242/26/1/014013

Lasing in subwavelength semiconductor nanopatches

Amit M Lakhani[1], **Kyoungsik Yu**[2] **and Ming C Wu**[1]

[1] Department of Electrical Engineering and Computer Sciences, University of California, Berkeley, CA 94720, USA
[2] Department of Electrical Engineering, Korea Advanced Institute of Science and Technology, Daejeon 305-701, Korea

E-mail: wu@eecs.berkeley.edu

Received 2 June 2010, in final form 27 July 2010
Published 24 November 2010
Online at stacks.iop.org/SST/26/014013

Abstract
Subwavelength semiconductor nanopatch lasers were analyzed, fabricated and characterized. Lasing was achieved in cylindrical and rectangular metallodielectric nanopatch geometries. The two smallest moderate quality factor modes of cylindrical cavities, the 'electric-' and 'magnetic-' dipole-like modes, successfully lased with physical volumes as small as $0.75\ (\lambda_0/n)^3$. Polarization control in nanopatch geometries is successfully demonstrated in anisotropic rectangular nanopatch structures.

1. Introduction

Since the invention of lasers in the 1960s, many different types of novel, interesting and useful coherent light sources have been developed for countless applications. The invention of semiconductor double heterostructures further propelled laser technology by allowing the creation of electrically injected lasers based on semiconductor materials [1]. Such lasers have been used in many applications including telecommunications, multimedia, sensing, etc. Recently, nanocavity lasers have attracted immense interest in many scientific communities due to their many potential applications in physics [2–4], imaging [5], sensing [6–9], data storage [10], optical interconnects [11–13], etc. For example, creating nanolasers capable of transmitting information with $\sim$1 fJ bit^{-1} of energy at high data rates will revolutionize current microprocessor technology [12]. Photodetectors that are capable of detecting such low powers with minimal energy consumption will need to be developed as well [14, 15].

The march to the creation of nanolasers has spanned many decades. Starting with the invention of the double heterostructure laser [1], the field has progressed in creating microcavity lasers such as vertical-cavity surface-emitting lasers (VCSELs) [16, 17], microdisks [18, 19] and photonic crystals [20, 21]. These cavities have succeeded in shrinking electromagnetic mode volumes down to the diffraction limit. Efforts to squeeze electromagnetic mode volumes down below the diffraction limit require metal. Thus far, some metal-based semiconductor lasers have been achieved by squeezing the mode volume of light in only two of three dimensions [22, 23]. Gold nanoparticles ($\sim$40 nm) have also shown stimulated emission using highly concentrated dye molecules as optical gain materials [24], and room-temperature optically pumped metallodielectric lasers have also been demonstrated with physical sizes on the order of $\sim$1 μm^3 [25]. These metallodielectric lasers represent a great start to achieving lasers with ultra-small mode volumes and physical sizes.

To be useful in optical interconnect applications, however, the physical size of nanolasers will need to be reduced further for highly dense integration with electronic transistors. To reduce the physical and electromagnetic modal size of nanocavities further, techniques used in the microwave community can be borrowed. The microstrip resonator used in antenna and filter applications provides a robust method of creating high quality factor cavities [26]. The use of patch cavities in the optical regime has been proposed and theoretically studied by Manalatou and Rana [27]. The paper focuses mainly on one cavity mode for this particular cavity geometry. However, using higher order modes can be beneficial in obtaining higher quality factors and engineering radiation patterns.

In this paper, the authors aim to demonstrate a versatile platform of realizing many different types of metallodielectric lasers. The fabrication methods developed can be extended for integration onto carrier substrates such as complementary metal-oxide–semiconductor (CMOS) chips.

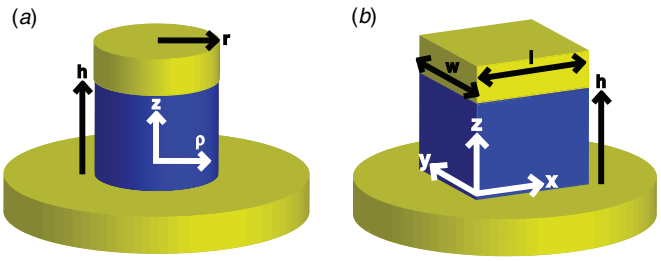

Figure 1. A schematic of (*a*) circular and (*b*) rectangular nanopatch cavities. Yellow regions represent gold and blue areas signify InGaAsP semiconductor gain media. White variables represent the coordinate system, and black variables represent cavity dimensions.

The metallodielectric cavities demonstrated include circular and rectangular nanopatch cavities. Each cavity shape has its own advantages, and they will be demonstrated throughout the paper. The basic geometry of nanopatch cavities can be seen in figure 1.

Because these lasers operate at near-infrared frequencies, metal behaves more ideally than at visible wavelengths so that plasmonic effects can be neglected and metals can be used in traditional roles (with lower conductivity). Using these metal-optic effects, lasing is achieved in two modes of the cylindrical resonator [28] and one mode of the rectangular nanopatch. Physical laser volumes as low as $V_{\text{phys}} = 0.75\ (\lambda_0/n)^3$ are achieved [28].

2. Analysis of nanopatch cavities

2.1. Model for nanopatch cavities

Nanocavities with metal covering the top and bottom and sidewalls exposed can be analyzed analytically using the first-order Cohn model [29], although quality factors cannot be obtained since the model assumes lossless metal. The model is found to approximately predict how cylindrical and rectangular nanocavities behave. In the model, the metal is assumed to be a perfect electrical conductor (PEC) with a variable skin depth associated with the amount of energy present in the real metal for a specific eigenmode. The semiconductor sidewall is assumed to be a perfect magnetic conductor (PMC). This particular approximation is excellent in the microwave regime, where dielectric constants can be extremely high [30]. Even at optical frequencies, this approximation can still yield good models for predicting the eigenenergies for many eigenmodes of nanopatch cavities.

2.1.1. Analysis of cylindrical nanopatch cavities. Starting from the Helmholtz equation, $(\nabla^2 + k^2)\vec{E} = 0$, a general solution in cylindrical coordinates is obtained:

$$E_{r,\varphi,z}(r,\varphi,z) = \sum_{m=0}^{\infty}\sum_{p=0}^{\infty}[\alpha_{mp}J_m(\eta\rho) + \gamma_{mp}Y_m(\eta\rho)] \times [c_m\cos(m\varphi) + d_m\sin(m\varphi)][f_p\,e^{-pz} + g_p\,e^{pz}], \quad (1)$$

where $\eta^2 = k^2 + p^2$, $k^2 = \omega^2\mu\varepsilon$, μ and ε are permeability and permittivity, m is the azimuthal mode number, p is the axial mode number (and eigenvalue), J_m is a Bessel function of the first kind and Y_m is a Bessel function of the second kind. Transverse magnetic (TM) and transverse electric (TE) solutions exist in nanopatch cavity structures. The mode propagation direction is defined to be in the z-direction (figure 1). The notation TM_{mnp} and TE_{mnp} can be used to annotate a particular eigenmode for any cylindrical nanopatch, where m, n and p represent the azimuthal, radial and axial mode numbers, respectively. The fundamental mode is the TM_{110} mode. However, this mode is an extremely efficient radiator and unsuitable for laser cavities. Thus, the next eigenmode, the TM_{111} mode, will be referred to as the 'fundamental' mode of the cylindrical nanopatch.

It is only necessary to solve for one field component (E_z for TM modes and H_z for TE modes) since the others can be obtained through Maxwell's equations. Mode profiles for the first two laser modes, TM_{111} [27] and TE_{011}, are

$$\text{TM}_{111}: \begin{cases} E_z = -E_0 J_1(\eta_{\text{TM}_{111}}\rho)\cos\left(\frac{\pi z}{h}\right)\sin(\phi) \\ \eta_{\text{TM}_{111}} = \sqrt{\left(2\pi/\lambda_{\text{TM}_{111}}\right)^2 - (\pi/h)^2} \end{cases}$$
$$\text{TE}_{011}: \begin{cases} H_z = H_0\eta_{\text{TE}_{011}}^2 J_0\left(\eta_{\text{TE}_{011}}\rho\right)\sin\left(\frac{\pi z}{h}\right) \\ \eta_{\text{TE}_{011}} = \sqrt{\left(2\pi/\lambda_{\text{TM}_{111}}\right)^2 - (\pi/h)^2} \end{cases}, \quad (2)$$

where h is the height of the cavity, and only one of the two degenerate TM_{111} modes is shown for simplicity. More generally, the eigenvalue spectra for TM [27] and TE modes in cylindrical cavities are

$$\lambda_{\text{TM}_{mnp}} = 2\pi\sqrt{\varepsilon}\left((\chi'_{mn}/r)^2 + \left(p\pi\Big/\left(h + 2\Delta_{\text{TM}_{mnp}}\right)\right)^2\right)^{-1/2}$$
$$\lambda_{\text{TE}_{mnp}} = 2\pi\sqrt{\varepsilon}\left((\chi_{mn}/r)^2 + \left(p\pi/\left(h + 2\Delta_{\text{TE}_{mnp}}\right)\right)^2\right)^{-1/2}, \quad (3)$$

where ε is the material's dielectric constant, χ_{mn} (χ'_{mn}) is the nth zero of the (derivative of the) mth Bessel function, p is the axial mode number and Δ_{mnp} is the skin depth associated with the mode's energy into the metal. From these general equations, dispersion relations relating cavity dimensions and eigenenergies can be found. In figure 2, the dispersion relation for different modes of cylindrical nanopatches is plotted. The analytical model agrees well with simulated structures as long as the height of cavities is tuned based on the 'effective skin depth' associated with a particular mode. Experimentally, only the TM_{111}, TE_{011} and TM_{011} cavity modes are observed (blue-shaded region), although the TM_{011} mode does not lase due to its low quality factor. Higher order modes can be obtained by designing thicker semiconductor layers and larger radii cavities.

2.1.2. Analysis of rectangular nanopatch cavities. Rectangular cavities behave similarly to cylindrical cavities, except that the eigenenergies are obtained using the Helmholtz equation in Cartesian coordinates. The modes of rectangular cavities can be labeled as TM_{abc}, where a, b and c represent mode numbers associated with the length (l), width (w) and height (h) of the cavity, respectively (figure 1). The TM_{a0c} mode has an electric field profile and eigenvalues:

$$\text{TM}_{a0c}: \begin{cases} E_z = E_0\cos\left(\frac{a\pi}{l}x\right)\cos\left(\frac{c\pi}{h}z\right) \\ E_x = E_0\frac{ac\pi^2}{hl\eta^2}\sin\left(\frac{a\pi}{l}x\right)\sin\left(\frac{c\pi}{h}z\right) \end{cases} \quad (4)$$

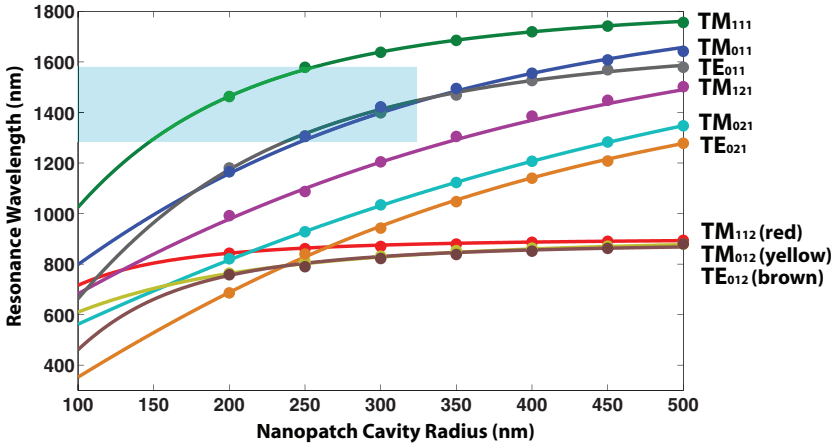

Figure 2. The theoretical (solid line) and simulated (points) dispersion of various eigenmodes of cylindrical cavities is shown. Good agreement is obtained between theory and simulation once effective skin depths are used. The shaded blue area represents the parameter space observed experimentally.

$$\lambda_{\mathrm{TM}_{abc}} = 2\pi\sqrt{\varepsilon}\left((a\pi/l)^2 + (b\pi/w)^2 + \left(c\pi/\left(h + 2\Delta_{\mathrm{TM}_{abc}}\right)\right)^2\right)^{1/2}, \quad (5)$$

where $\eta^2 = \mu\varepsilon\omega^2{}_{a0c} - (c\pi/h)^2$, $\Delta_{\mathrm{TM}_{abc}}$ is the 'effective skin depth' of the fundamental mode of the rectangular cavity and only x-polarized mode profiles are shown for simplicity. TE modes also exist in rectangular patch geometries; however, only the fundamental TM mode of such cavities will be shown. Rectangular cavities can be especially interesting given that anisotropic devices can be used to control the polarization of light that is emitted by a TM mode. Rectangular cavities can also be used to resonantly pump nanopatch cavities [31]. Since nanopatch cavities are subwavelength, pumping schemes require the structure to be resonant at the pump wavelength for efficient transfer of energy. The rectangular cavity can be designed with anisotropy, so that one polarization has a cavity resonance at the desired emission wavelength, and the other polarization has a strong resonance at the pump frequency. Resonant pumping schemes can drastically reduce pump-induced heating by making the cavity couple more efficiently to the excitation source.

2.2. Simulation of nanopatch cavities

Along with finding the eigenenergies of different cavity modes, mode profiles were also simulated using two-dimensional finite-element method (FEM) techniques [32]. The electric and magnetic energy densities for various modes of cylindrical cavities are shown in figure 3. Generally, the TM modes have field lines that terminate in metal, causing large metal absorption. These modes can be more clearly understood as charge distributions in the metal that create certain mode configurations. For example, the TM_{111} can be viewed as two oscillating electric dipoles ('electric-dipole-like') in the top metal patch and bottom ground plane. These dipoles add constructively in the semiconductor region. In the far-field, however, the two dipoles cancel in the vertical direction because they are about one-half wavelength apart from each other (due to the 220 nm of semiconductor between them) and therefore create a good nanocavity. TE modes are magnetic in nature, and have only azimuthal electric fields. These modes can also be mapped to different current distributions in the metal layers, causing differing amounts of radiation and loss. The TE_{011} mode is called the 'magnetic-dipole-like' mode due to the azimuthal displacement current present in the semiconductor.

The quality factors, confinement factor and mode volume of each eigenmode were also simulated using finite difference time domain (FDTD) simulations. Different cavities were simulated with silver and gold as the metal layers. The total ($Q_{\mathrm{tot,Ag}}$, $Q_{\mathrm{tot,Au}}$), radiation (Q_{rad}) and loss ($Q_{\mathrm{abs,Ag}}$, $Q_{\mathrm{abs,Au}}$) quality factors are calculated for each metal. The confinement factor $\Gamma = \int_{\mathrm{gain}}\varepsilon(\boldsymbol{r})|\boldsymbol{E}(\boldsymbol{r})|^2 d^3\boldsymbol{r}/\int_{\mathrm{all}}\varepsilon(\boldsymbol{r})|\boldsymbol{E}(\boldsymbol{r})|^2 d^3\boldsymbol{r}$ and normalized electromagnetic mode volume $V_n = V_{\mathrm{mode}}/(\lambda_0/n)^3$ (where $V_{\mathrm{mode}} = \int\varepsilon(\boldsymbol{r})|\boldsymbol{E}(\boldsymbol{r})|^2 d^3\boldsymbol{r}/\max(\varepsilon(\boldsymbol{r})|\boldsymbol{E}(\boldsymbol{r})|^2)$ are also found for each eigenmode. A summary of the above figures of merit is shown in table 1 for cylindrical cavity eigenmodes. The TM_{111} and TM_{012} modes have the highest radiation quality factors and can be extremely good laser cavities if silver is used. The TE modes radiate well, and the efficiency of these modes can also be good since the absorption and radiation quality factors are well matched. Also, in general, TM modes with odd parity ($m = 1$) have the smallest mode volumes, and TE modes have the largest mode volumes.

3. Fabrication methods

Metallodielectric nanocavities present a unique fabrication challenge. At the nanoscale, surface recombination in semiconductors becomes a dominant recombination mechanism, reducing laser efficiency. Furthermore, metal–semiconductor integration presents another loss mechanism. Mindful of the effects of surface recombination on nanocavity laser performance, the best material with a bandgap in the near-infrared is the $\mathrm{In}_x\mathrm{Ga}_{1-x}\mathrm{As}_y\mathrm{P}_{1-y}$ quaternary material

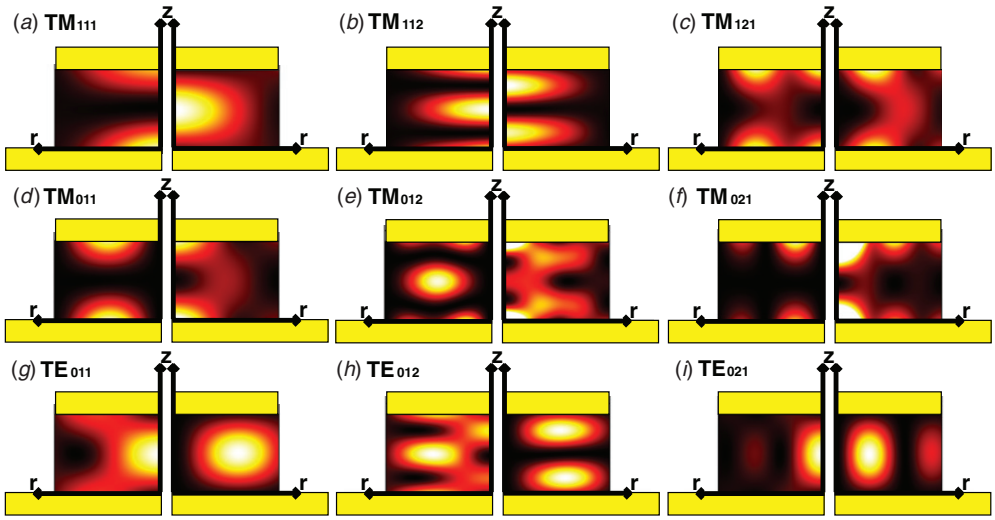

Figure 3. Magnetic (left) and electric (right) energy densities of various eigenmodes of cylindrical nanopatch cavities are shown. The first row shows modes with odd parity ($m = 1$), the second and third rows shows modes with no angular dependence ($m = 0$). The first two rows show TM modes while the second row shows TE modes. Each mode profile is labeled according to the mode it represents.

Table 1. Summary of pertinent cavity parameters for various eigenmodes of cylindrical nanopatches.

	TM_{111}	TM_{112}	TM_{121}	TM_{021}	TM_{012}	TE_{011}	TE_{012}
$Q_{\text{tot,Ag}}$	250	350	116	155	460	143	240
$Q_{\text{tot,Au}}$	65	120	61	62	128	80	128
Q_{rad}	1600	500	167	298	3000	205	325
$Q_{\text{abs,Ag}}$	295	100	380	323	540	473	917
$Q_{\text{abs,Au}}$	68	150	96	78	133	131	211
Γ	0.84	0.93	0.62	0.70	0.90	0.89	0.95
V_n	0.067	0.146	0.169	0.081	0.8	0.374	0.875

system, which has a surface recombination velocity $v_s \sim 2 \times 10^4$ cm s^{-1} [33] (roughly two orders of magnitude slower than GaAs systems). $In_xGa_{1-x}As_yP_{1-y}$ can also have high-energy barriers to confine carriers and prevent thermalization into metal. In this paper, a very thin layer of titanium dioxide was used to prevent carrier recombination in metal layers. However, the thickness of this dielectric can have significant impacts on device performance. If the oxide is too thick, the confinement factor of the eigenmode is reduced and more gain is required to initiate lasing. If the dielectric is too thin, then carriers can tunnel through the dielectric, degrading photoluminescence and the laser's efficiency. After careful study into optimum dielectric design, 5 nm of titanium oxide was chosen to maximize the mode confinement factor, although efficiency is reduced. The dependence of semiconductor photoluminescence on oxide thickness can be seen in figure 4. In the future, large bandgap semiconductors will be used instead of oxide to confine carriers, enabling electrical injection.

The nanolasers were fabricated using a process that can be compatible with integration onto silicon substrates for applications in optical interconnect technology. In summary, oxide and metal are evaporated onto the epitaxial layer, the

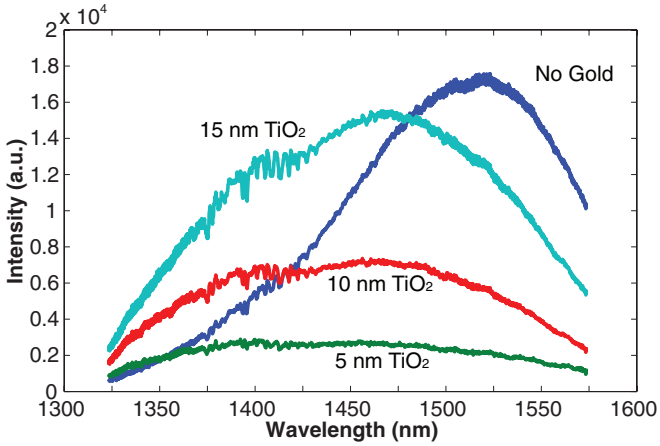

Figure 4. The dependence of photoluminescence (PL) from a 220 nm thick epitaxial layer of InGaAsP with varying thicknesses of titanium dioxide between semiconductor and gold is shown. The data were taken after step (d) in the fabrication process shown in figure 5 at room temperature under pulsed (100 ns, 20 kHz repetition rate) and high-power pumping conditions. The reason for the anomalous PL present at 1400 nm was not studied, although Fabry–Pérot resonances in the thin film structure that was probed could cause such enhancement. The PL degrades as the oxide thickness decreases, signifying that carriers are tunneling into the metal from the semiconductor. At 15 nm of TiO_2, the peak PL reaches nearly the same intensity as a semiconductor layer without any metal present.

substrate is then flipped upside down and bonded to another carrier, mechanical grinding and wet etching techniques are used to remove the backside, the sample is patterned using electron-beam lithography and liftoff, and the semiconductor is finally etched using reactive ion etching (figure 5). Scanning electron micrographs of nanopatch cavities can also be seen in figure 6. More details of the fabrication process can be found elsewhere [28].

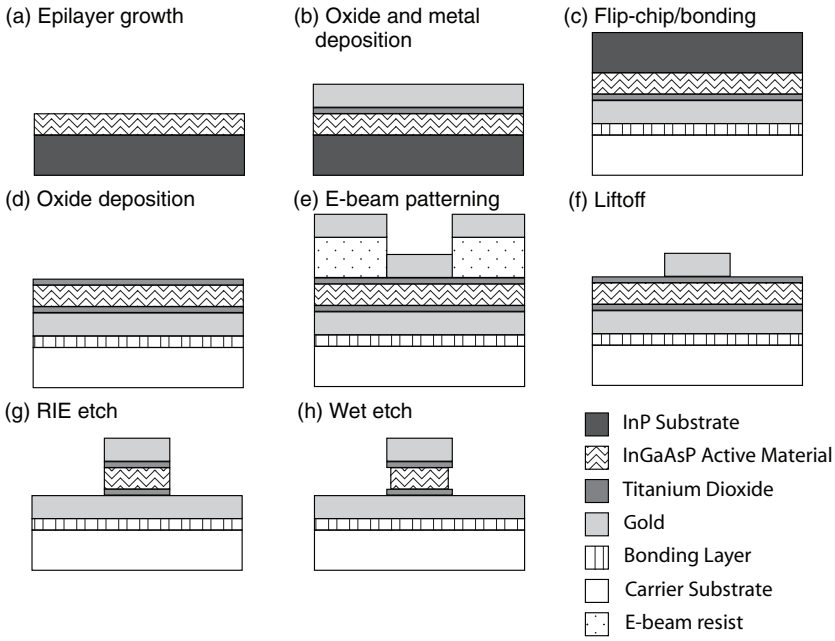

Figure 5. Side view of a typical fabrication flow for creating nanopatch cavity lasers.

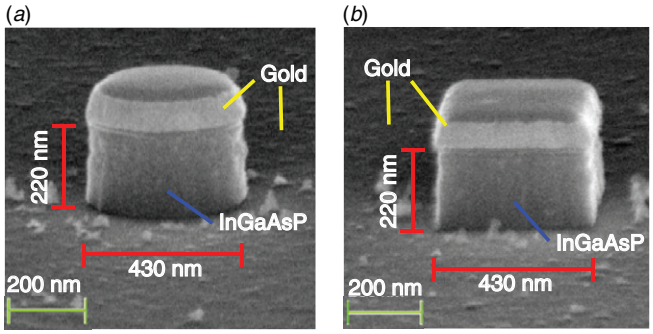

Figure 6. Scanning electron micrographs of fabricated nanopatch lasers after reactive ion etching. Perspective views (65° tilt) of cylindrical and rectangular nanopatches are seen in (*a*) and (*b*), respectively.

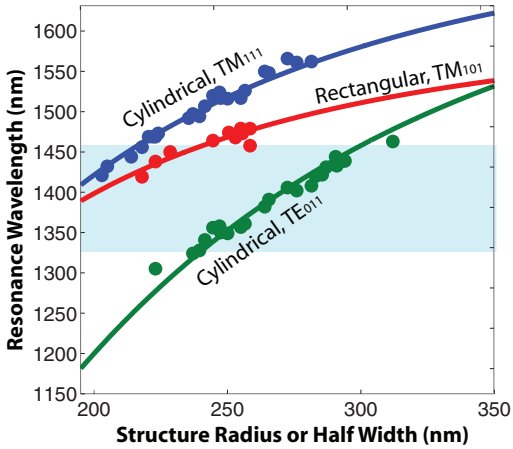

Figure 7. The dependence of cavity geometry on resonance wavelength is shown. For cylindrical (rectangular) cavities, the horizontal axis represents cavity radius (half-width). The blue-shaded region indicates the gain bandwidth of the semiconductor where lasing is observed. Dots represent experimental data.

4. Results and discussion

The semiconductor nanolasers were measured and characterized using a micro-photoluminescence setup with a pulsed (100 ns, 5 kHz repetition rate) 1064 nm pump laser (more details can be found elsewhere [28]). The lasers were probed using optical pumping at 77 Kelvin. Rate equations from Coldren and Corzine [34] were used to analyze the pump-dependent power output (L–L curve) relationship of the devices. In these nanocavities, the effects of spontaneous emission are also modeled. The increase in the speed of spontaneous emission is quantified by the Purcell factor ($F = (16/\pi^2)Q/V_n$), and the fraction of spontaneous emission that is coupled to the laser mode is called β.

Lasing from multiple modes of nanopatch cavities is observed. Since the height of the cavities is fixed at 220 nm (due to the epiwafer that was used), lasing is observed from TM_{111} and TE_{011} modes for cylindrical geometries and TM_{011} and TM_{101} modes for rectangular geometries. Experimentally, the dependence of resonance wavelength on size agrees well with theory as seen in figure 7. With other cavity heights, it will be possible to see laser emission from even higher order cavity modes, such as the ones theorized and simulated in figure 2. Again, different mode configurations can lead to different applications since far-field patterns for each mode are different.

In cylindrical geometries, the TM_{111} mode is of great interest, since it represents a laser mode with a sub-diffraction limited mode and physical volumes ($V_n = 0.067$, $V_{\text{phys}} = 0.75$). This so-called electric dipole mode is also the most fundamental moderate quality factor mode in a cylindrical nanopatch laser. Experimentally, the quality factor is

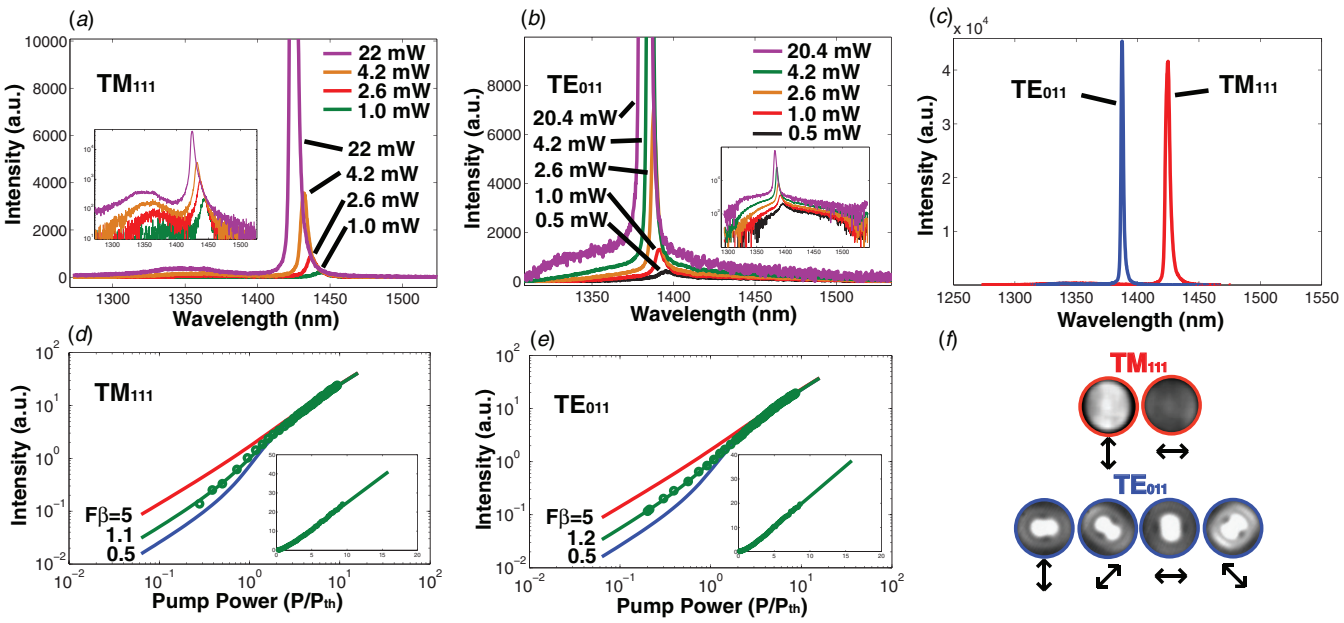

Figure 8. Pump-dependent spectra are shown in linear- and log-scale (inset) for the (*a*) TM_{111} and (*b*) TE_{011} cylindrical cavity modes. The linewidths measured are resolution limited (2 nm resolution bandwidth) above threshold. Linear scale spectra from the two modes after threshold are seen in (*c*). Pump-dependent power outputs of nanopatch lasers are seen in (*d*) and (*e*) where rate equation modeled L–L curves are overlaid; $F\beta = 5$ and $F\beta = 0.5$ curves are also shown for comparison to the best-fitted model for each mode. Polarization-dependent near field images of each mode confirm each mode's identity, with the TM_{111} mode being linearly polarized, and the TE_{011} mode being azimuthally polarized.

measured to be $Q_{exp} = 132$. The TM_{111} mode has surface normal light emission, much like a VCSEL, and is linearly polarized due to its odd parity. The TE_{011} mode, also called the 'magnetic dipole' mode since the electric field lines only have an azimuthal component, also lases. The magnetic mode has a larger mode volume and physical size ($V_n = 0.375$, $V_{phys} = 1.25$) compared to the TM_{111} mode. Experimentally, the quality factor is measured to be $Q_{exp} = 168$. It emits most of its radiation parallel to the gold ground plane, making it very useful for integration into nanophotonic circuits. Temperature-dependent quality factors suggest that metal loss is reduced at low temperatures [22]. Large coupling of Purcell-enhanced spontaneous emission is also observed in both modes. Purcell factors for the TM_{111} and TE_{011} modes were calculated to be $F \sim 50$ and $F \sim 11$, respectively. The L–L curves obtained experimentally were fit best with theory using $F\beta$ factors of $F\beta = 1.1$ and $F\beta = 1.2$ for the TM_{111} and TE_{011} modes, respectively (figure 8). Thus, the fraction of spontaneous emission coupled to the laser mode, β, was calculated to be $\beta = 0.022$ and $\beta = 0.105$ for the TM_{111} and TE_{011} modes, respectively. Data taken from cylindrical nanopatch lasers are summarized in figure 8.

Rectangular nanopatches also show lasing action. Two non-degenerate modes with 'electric-dipole-like' mode profiles are seen if the rectangle is anisotropic (the length is different from the width of the cavity). These devices also have vertical radiation emission. These modes eventually become degenerate as the anisotropy between the length and the width is reduced (figure 9). Between the two modes, the higher energy mode always lases since higher gain can be achieved at higher energies due to a larger density of states. A plot of the mode spacing versus anisotropy ratio is seen in figure 9(*f*). There is an overall red shift in cavity resonances only because the cavities probed had larger dimensions at lower anisotropy. The spectra recorded in figure 9 are slightly above lasing threshold so that both modes can be seen clearly. At larger pumping powers, the higher energy mode becomes the dominant mode, and spontaneous emission becomes clamped.

To verify that the two modes seen in figure 9 were 'electric-dipole-like,' the polarization dependence of the two modes was studied. The two modes under study are the TM_{011} and the TM_{101} modes, which have orthogonal polarizations. They should also be linearly polarized, since the radiation can be thought of as coming from two electric dipoles in the metal layers of the cavity structure. In figure 10, an anisotropic rectangular nanopatch is probed with a linear polarizer below laser threshold. As the polarizer is rotated through 180°, only one of the two modes is seen if the polarization is horizontal or vertical to the rectangle (figures 10(*a*) and (*c*), respectively). At diagonal polarizations, both modes appear (figures 10(*b*) and (*d*)). Thus, each mode is strongly linearly polarized. Since these modes are the fundamental moderate quality factor modes of rectangular cavities, they are useful for ultra-small laser designs. Unlike circular nanopatches, however, the polarization of the cavity can be controlled with great precision. Control over polarization in nanocavities can lead to many different applications including display technologies and quantum information processing.

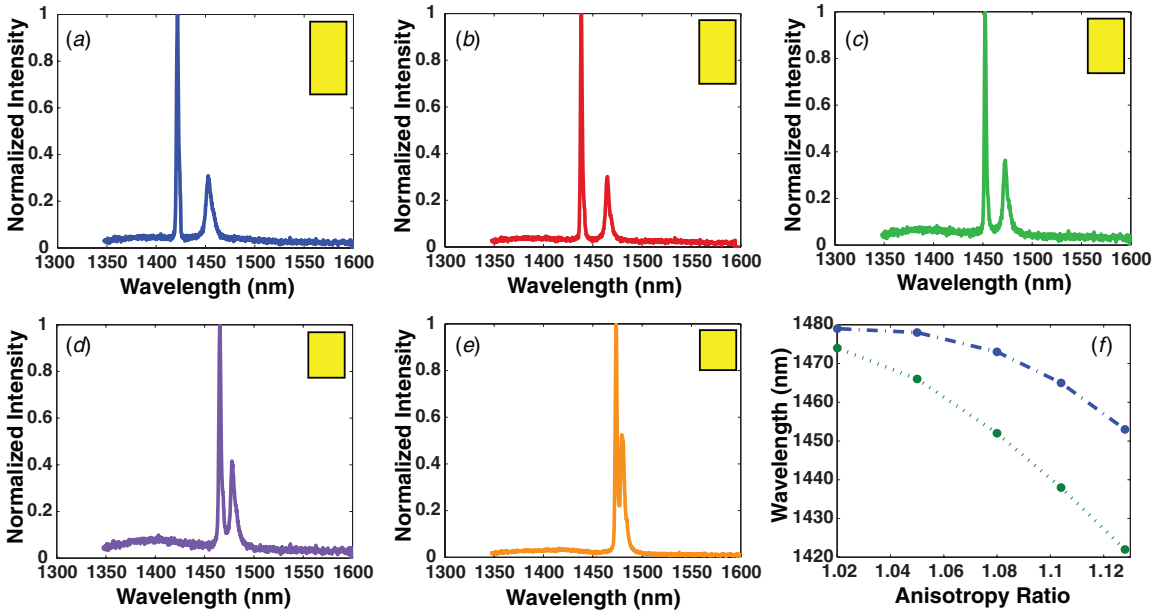

Figure 9. Nearly lasing spectra for rectangular patches with different anisotropy ratios are shown. The anisotropy ratio is reduced in order from (*a*) to (*e*). The yellow rectangles in the corner of each graph signify the top view of each rectangular nanopatch cavity, where the anisotropy has been exaggerated for clarity. The mode separation and wavelength versus anisotropy ratio is seen in (*f*).

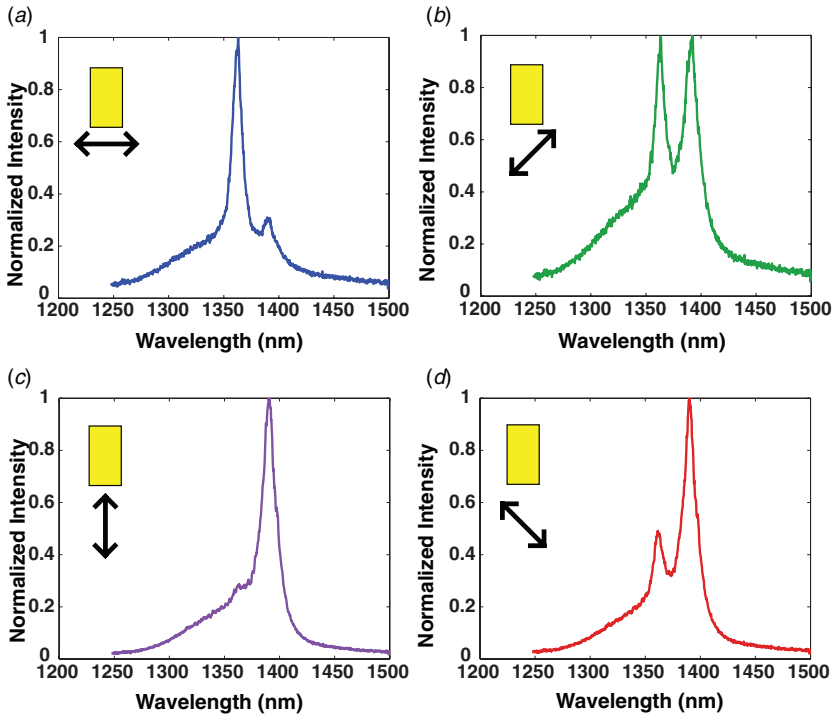

Figure 10. The two distinct resonances of an anisotropic rectangular cavity are shown below lasing threshold to have orthogonal polarizations. The yellow square represents the geometry of the cavity in the *x*–*y* plane. The arrows represent the *approximate* polarization of the spectrum shown in each viewgraph, therefore graphs (*b*) and (*d*) have slightly different peak heights.

5. Conclusion

Nanopatch lasers of varying geometries were analyzed, simulated, fabricated and characterized. These lasers operate at near-infrared wavelengths and can be smaller than the diffraction limit in both modal and physical volumes. Using metallodielectric cavities at optical frequencies, radiation can be suppressed compared to purely dielectric cavities of similar dimensions. Although loss is incurred with the presence of metal, using silver should help mitigate these problems. These lasers can also serve as attractive devices to investigate phenomena related to strong light–matter interactions. More importantly, however, they are physically small and easily

adaptable to electrical injection, making them attractive candidates for future integration onto silicon electronics.

Acknowledgments

The authors would like to acknowledge DARPA NACHOS, NSF CIAN-ERC and the Samsung Global Research Outreach program for funding. This material is based upon work supported under a National Science Foundation Graduate Research Fellowship. The authors would also like to acknowledge Erwin K. Lau, Myung-Ki Kim and Michael S. Eggleston for helpful discussions. Finally, the authors acknowledge the Berkeley Microlab for their fabrication support.

References

[1] Alferov Z I 2001 Nobel Lecture: the double heterostructure concept and its applications in physics, electronics, and technology *Rev. Mod. Phys.* **73** 767
[2] Nomura M, Kumagai N, Iwamoto S, Ota Y and Arakawa Y 2010 Laser oscillation in a strongly coupled single-quantum-dot-nanocavity system *Nat. Phys.* **6** 279–83
[3] Reithmaier J P *et al* 2004 Strong coupling in a single quantum dot—semiconductor microcavity system *Nature* **432** 197–200
[4] Gerard J M, Sermage B, Gayral B, Legrand B, Costard E and Thierry-Mieg V 1998 Enhanced spontaneous emission by quantum boxes in a monolithic optical microcavity *Phys. Rev. Lett.* **81** 1110
[5] Nakayama Y *et al* 2007 Tunable nanowire nonlinear optical probe *Nature* **447** 1098–101
[6] Asher S A *et al* 2003 Photonic crystal carbohydrate sensors: low ionic strength sugar sensing *J. Am. Chem. Soc.* **125** 3322–9
[7] Loncar M, Scherer A and Qiu Y 2003 Photonic crystal laser sources for chemical detection *Appl. Phys. Lett.* **82** 4648
[8] Alivisatos P 2003 The use of nanocrystals in biological detection *Nat. Biotechnol.* **22** 47–52
[9] Boyd R W and Heebner J E 2001 Sensitive disk resonator photonic biosensor *Appl. Opt.* **40** 5742–7
[10] Challener W A *et al* 2009 Heat-assisted magnetic recording by a near-field transducer with efficient optical energy transfer *Nature Photonics.* **3** 220–4
[11] Meindl J D, Davis J A, Zarkesh-Ha P, Patel C S, Martin K P and Kohl P A 2002 Interconnect opportunities for gigascale integration *IBM J. Res. Dev.* **46** 245
[12] Miller D 2009 Device requirements for optical interconnects to silicon chips *Proc. IEEE.* **97** 1166–85
[13] Lau E K, Lakhani A, Tucker R S and Wu M C 2009 Enhanced modulation bandwidth of nanocavity light emitting devices *Opt. Express.* **17** 7790–9
[14] Tang L *et al* 2008 Nanometre-scale germanium photodetector enhanced by a near-infrared dipole antenna *Nat. Photon.* **2** 226–9
[15] Ishi T, Fujikata J, Makita K, Toshio B and Ohashi K 2005 Si nano-photodiode with a surface plasmon antenna *Jpn. J. Appl. Phys.* **44** L364–L366
[16] Iga K, Koyama F and Kinoshita S 1988 Surface emitting semiconductor lasers *IEEE J Quantum Electron.* **24** 1845–55
[17] Jewell J L, Harbison J P, Scherer A, Lee Y H and Florez L T 1991 Vertical-cavity surface-emitting lasers: design, growth, fabrication, characterization *IEEE J. Quantum Electron.* **27** 1332–46
[18] McCall S L, Levi A F J, Slusher R E, Pearton S J and Logan R A 1992 Whispering-gallery mode microdisk lasers *Appl. Phys. Lett.* **60** 289
[19] Baba T 1997 Photonic crystals and microdisk cavities based on GaInAsP-InP system *IEEE J. Sel. Top. Quantum Electron.* **3** 808–30
[20] Painter O *et al* 1999 Two-dimensional photonic band-gap defect mode laser *Science* **284** 1819–21
[21] Nomura M *et al* 2006 Room temperature continuous-wave lasing in photonic crystal nanocavity *Opt. Express.* **14** 6308–15
[22] Hill M T *et al* 2007 Lasing in metallic-coated nanocavities *Nature Photon.* **1** 589–94
[23] Oulton R F *et al* 2009 Plasmon lasers at deep subwavelength scale *Nature* **461** 629–32
[24] Noginov M A *et al* 2009 Demonstration of a spaser-based nanolaser *Nature* **460** 1110–2
[25] Nezhad M P *et al* 2010 Room-temperature subwavelength metallo-dielectric lasers *Nat. Photon.* **4** 395–9
[26] Caver K and Mink J 1981 Microstrip antenna technology *IEEE Trans. Antennas Propag.* **29** 2–24
[27] Manolatou C and Rana F 2008 Subwavelength nanopatch cavities for semiconductor plasmon lasers *IEEE J. Quantum Electron.* **44** 435–47
[28] Yu K, Lakhani A and Wu M C 2010 Subwavelength metal-optic semiconductor nanopatch lasers *Opt. Express.* **18** 8790–9
[29] Cohn S B 1968 Microwave bandpass filters containing high-Q dielectric resonators *IEEE Trans. Microw. Theory Tech.* **16** 218–27
[30] Kajfez D and Guillon P 1986 *Dielectric Resonators* (Dedham, MA: Artech House)
[31] Zhu Z H *et al* 2009 Optically pumped nanolaser based on two magnetic plasmon resonance modes *Appl. Phys. Lett.* **94** 103106
[32] Oxborrow M 2007 Traceable 2-d finite-element simulation of the whispering-gallery modes of axisymmetric electromagnetic resonators *IEEE Trans. Microw. Theory Tech.* **55** 1209
[33] Boroditsky M *et al* 2000 Surface recombination measurements on III–V candidate materials for nanostructure light-emitting diodes *J. Appl. Phys.* **87** 3497
[34] Coldren L A, Corzine S W and Coldren L A 1995 *Diode Lasers and Photonic Integrated Circuits* (New York: Wiley)